Mathematical modelling of glioma growth: The use of Diffusion Tensor Imaging (DTI) data to predict the anisotropic pathways of cancer invasion

K.J. Painter [a,*], T. Hillen [b]

[a] Department of Mathematics and Maxwell Institute for Mathematical Sciences, Heriot-Watt University, Edinburgh EH14 4AS, UK
[b] Centre for Mathematical Biology, Department of Mathematical and Statistical Sciences, University of Alberta, Edmonton, Canada T6G2G1

HIGHLIGHTS

► A multiscale model of glioma invasion along the aligned neural fibre tracts is presented.
► Diffusion tensor imaging (DTI) data is connected to parameters of the macroscopic model.
► We show the impact of alignment on the invasion pathways using synthetic and real DTI datasets.

ABSTRACT

The nonuniform growth of certain forms of cancer can present significant complications for their treatment, a particularly acute problem in gliomas. A number of experimental results have suggested that invasion is facilitated by the directed movement of cells along the aligned neural fibre tracts that form a large component of the white matter. Diffusion tensor imaging (DTI) provides a window for visualising this anisotropy and gaining insight on the potential invasive pathways. In this paper we develop a mesoscopic model for glioma invasion based on the individual migration pathways of invading cells along the fibre tracts. Via scaling we obtain a macroscopic model that allows us to explore the overall growth of a tumour. To connect DTI data to parameters in the macroscopic model we assume that directional guidance along fibre tracts is described by a bimodal von Mises–Fisher distribution (a normal distribution on a unit sphere) and parametrised according to the directionality and degree of anisotropy in the diffusion tensors. We demonstrate the results in a simple model for glioma growth, exploiting both synthetic and genuine DTI datasets to reveal the potentially crucial role of anisotropic structure on invasion.

© 2013 Elsevier Ltd. All rights reserved.

1. Introduction

Gliomas—tumours arising from the glial cells of the central nervous system (CNS)—form an often invasive class of tumours with poor prognosis following their anaplastic transformation. A severe impediment to their treatment is the diffuse and heterogeneous rate of invasion that leads to an "invisible" outer tumour, undetectable under current imaging resolution. This heterogeneous pattern of spread has, partly, been attributed to the anisotropic invasion of glioma cells along aligned structures in the brain, such as the bundled neural fibre tracts characteristic of white matter (Giese et al., 1996, 2003; Clatz et al., 2005; Bondiau et al., 2008; Konukoglu et al., 2010; Jbabdi et al., 2005).

Diffusion tensor imaging (DTI), discussed in Section 2, is an imaging technique which measures the anisotropic diffusion of water molecules in a tissue. The alignment in highly structured tissues, such as the brain, muscles and bones, is revealed in the anisotropy of these diffusion tensors and, in the context of the brain, DTI can therefore map the pathways of neural fibre tracts and help construct an atlas of the brain's white matter architecture (Basser, 2008). Given the hypothesised invasion of glioma cells along fibre tracts, DTI therefore has the potential to predict tumour expansion and guide therapy.

Mathematical/computational modelling provides one approach for forecasting these invasive pathways and a number of macroscopic models have been developed which employ DTI data to inform the white matter architecture and simulate the nonuniform growth of a glioma, e.g. Clatz et al. (2005); Jbabdi et al. (2005); Cobzas et al. (2009); Konukoglu et al. (2010); and Mosayebi et al. (2011). Unexplored questions within this modelling, however, include (1) connecting the DTI data/local tissue architecture to an individual-level model for the invasive pathway of the cancer cell and (2) how to then scale this model into a macroscopic model for tumour growth. In this paper we present a method for exploring these questions by first formulating a transport equation and then employing scaling arguments to derive the corresponding macroscopic model. Transport equations are

* Corresponding author. Tel.: +44 131 4518234; fax: +44 131 4513249.
   E-mail addresses: K.Painter@hw.ac.uk (K.J. Painter),
thillen@ualberta.ca (T. Hillen).

fundamentally based on the characteristic pathways of individual cell movement, parametrised according to "measurable" properties such as velocities, turning rates and turning angles. Scaling leads to macroscopic equations in the form of anisotropic reaction–diffusion equations and we apply these models to artificial and genuine DTI datasets to show the utility of this approach.

1.1. Modelling anisotropic invasion

Predicting the rate and pattern of spread of an invasive cancer as it infiltrates healthy tissue is fundamental for delivering an effective and targeted treatment. Paramount to this goal is uncovering the various navigational cues that govern the migratory pathways of cells. One such determinant can be found in the structure of the environment (or substrate) through (or on) which the cells are moving: the directional movement of cells in response to aniso-tropy in the environment, termed *contact guidance* (Dunn and Heath, 1976; Guido and Tranquillo, 1993). Aligned migration of cells is a common characteristic, found in processes ranging from embryonic development to immune cell guidance, wound healing, and, of course, cancer invasion (Haston et al., 1983; Wood and Thorogood, 1984; Wolf et al., 2003). Environmental anisotropy is a widespread feature of tissues, stemming from the ordered align-ment of collagen fibres in connective tissues, the network structure of the blood vasculature and lymphatic system and the bundling of nerve fibre tracts in the white matter of the central nervous system.

Mathematical modelling of cell migration and tumour invasion has developed significantly over recent years and a range of models have been specifically developed with glioma growth and treatment in mind, e.g. see the reviews of Swanson et al. (2003), Hatzikirou et al. (2005), and Mandonnet et al. (2008). A significant number of these studies have concentrated on the macroscopic process of glioma expansion, employing relatively simple equations of reaction–diffusion type to model the evolving density of glioma cells, $c(\mathbf{x},t)$, where $\mathbf{x}$ describes the position in the CNS and t denotes time:

$$c_t = \nabla(D_C(\mathbf{x},t)\nabla c) + f(c,\mathbf{x},t). \qquad (1)$$

Terms on the right hand side, respectively, model the spatial expansion or invasion of the tumour and cell proliferation. While earlier models assumed isotropic and homogeneous growth, setting D_C to be a scalar and constant diffusion coefficient, later models have taken into account an impact from the complex tissue structure on invasion. For example, Swanson et al. (2000) consid-ered a spatially heterogeneous diffusion coefficient, setting D_C to be significantly higher in white over grey matter to describe the faster invasion observed in these regions. Critically, modelling was matched to clinical data to optimise parameter selection and extensions have included exploring radiation and chemotherapy treatments, glioma classification, glioma evolution and tumour–host interactions (e.g. Swanson et al., 2003; Hatzikirou et al., 2005).

Other models have expanded further on the form of the invasion term in (1). A mathematical–mechanical model for glioma invasion has been developed in Clatz et al. (2005), Bondiau et al. (2008), and Konukoglu et al. (2010), dividing the tumour extent into two parts. One portion describes the main tumour mass, including the solid tumour core, and is modelled as a viscoelastic tissue which grows and pushes on the surrounding medium, leading to its deformation. The second component includes the invasive region, along with the invisible outer tumour extent, and is modelled by a reaction–diffusion equation of the form (1). The diffusion coefficient $D_C(\mathbf{x},t)$ is taken here to be an anisotropic diffusion tensor informed by DTI, with the anisotropy in $D_C(\mathbf{x},t)$ at $\mathbf{x}$ modelling the preferred invasion of cells along the white matter tracts. In these studies D_C is simply taken to be directly proportional to the measured water diffusion tensor obtained by DTI, yet it is

acknowledged that there is no sound biological justification for such a relationship, stating on p.1339 of Clatz et al. (2005) that "*the comparison of the influence of anisotropy on the diffusion of water molecules versus tumour cells has not been studied yet*". The above authors use brain atlas and real patient data to show the usefulness of their model. In particular, new treatment margins are suggested based on their mathematical model (Konukoglu et al., 2010).

Jbabdi et al. (2005) have also utilised DTI data within anisotropic diffusion models to predict glioma spread. The authors do not include mass effects, as in Clatz et al. (2005), however, do propose a more elaborate geometric argument to connect the water diffusion tensor measured by DTI, D_{Tl}, with the tumour cell diffusion tensor in a model of the form (1). By measuring the shape and degree of anisotropy in D_{Tl} the authors suggest a tumour diffusion tensor with its same orientation but parametrised by a tuning parameter which enhances or reduces the anisotropy of D_{Tl}. Matching to clinical data indicated that enhancement was required, yet key questions remain: How can this be more formally connected via an individual tumour cell's response to anisotropy and what form should the corresponding macroscopic model take?

Cobzas et al. (2009) and Mosayebi et al. (2011) propose using the DTI tensor to define a new metric on the brain domain, based on geometrical constructions of Lenglet et al. (2004) and O'Dennell et al. (2002) for connective white matter tissue. In normal treat-ment practice a 2 cm margin surrounding the visible lesion defines the treatment volume, mathematically corresponding to a 2 cm margin in the Euclidean metric. Cobzas et al. (2009) and Mosayebi et al. (2011) suggest a new metric G based on DTI data and compute the corresponding "2 cm" margin according to this new metric, which will extend or shorten the Euclidean distance according to the local DTI data. Aided by mathematical modelling, early explora-tions indicate that the new volume could potentially outperform the normal practice, although further analysis is undoubtedly required. For example, "*More robust methods for TDT extraction are required*" (where *TDT* is our D_C), see p. 371 of Mosayebi et al. (2011).

1.2. Outline

In each of the above studies a clear need for realistic and transparent connections between water diffusion, brain geometry and tumour cell invasion is indicated. Our aim is to present a systematic approach for these connections, based on transport equations for cell movement, scaling limits and the von Mises–Fisher distribution. In recent work (Hillen, 2006; Painter, 2009; Hillen and Painter, 2013) we developed transport equations as models for cell movement in aligned tissues. The transport equation formalism allows a detailed, microscopic description for the inter-actions of cells with the tissue fibres, as well as changes in their arrangement. The model was first developed in the context of mesenchymal cell migration in collagen networks however has been developed further in both mathematical theories (e.g. Hillen et al., 2010) and various applications (e.g. Kettemann, 2010; Hillen and Painter, 2013). To obtain macroscopic models in the form of reaction–advection–diffusion equations, scaling limits can be applied (Hillen and Painter, 2013). A key feature is that the microscopic properties of the cell–tissue interaction can be instantly translated into macroscopic parameters; in the present case we can connect a proposed model for cell invasion along the fibre tracts into an anisotropic diffusion tensor for the macroscopic cell density. Fig. 1 illustrates the modelling workflow.

In the next section we briefly review some salient mathema-tical facts concerning anisotropic diffusion, diffusion tensors and DTI. Section 3 reviews essential details concerning the transport model of Hillen (2006) and their scaling limits. In Section 4 we propose some specific algorithms that connect the data derived from DTI to the inputs for the invasion model. We directly apply
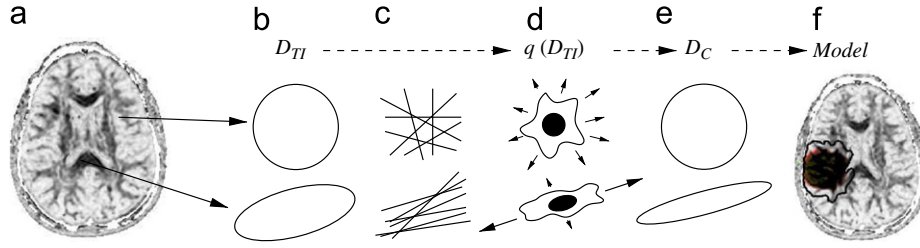
Fig. 1. Schematic for the translation between DTI data and a macroscopic model of glioma invasion; more information provided in the indicated sections. (a) DTI provides a spatial map for the anisotropic diffusion of water molecules (Section 2). Anisotropy plotted in terms of fractional anisotropy, from isotropic (white) to highly anisotropic (black). (b) Local anisotropy in a water diffusion tensor, D_{TI}, is represented by its anisotropy ellipsoid, examples shown corresponding to almost isotropic and anisotropic tensors (Section 2). (c) Local fibre tract architecture implied by these diffusion tensors. (d) We specify the cell turning function, q, for an individual-level model according to D_{TI} measures (e.g. fractional anisotropy, eigenvectors), see Sections 3 and 4. Note that the model directly translates D_{TI} into q, rather than explicitly defining a fibre structure. (e) Scaling the individual-model generates a macroscopic model of invasion, with the spatially varying cell diffusion tensor D_C depending on q (and hence D_{TI}), see Sections 3 and 4. (f) Simulations of the model predict anisotropic invasion (Section 5).
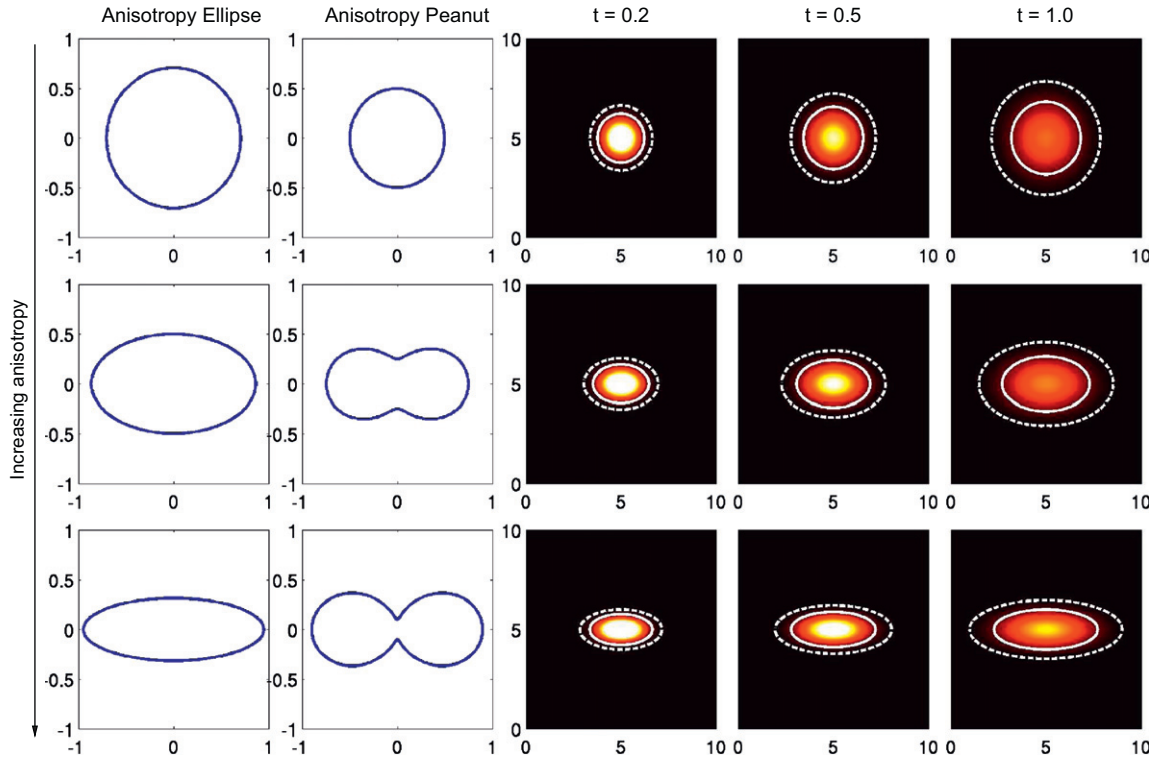

Fig. 2. Representations of anisotropic diffusion tensors and solutions of (2). In each row we plot (from left to right) the anisotropy ellipse, the anisotropy peanut and solutions to (2) at the times indicated. Top row: isotropic case, $D = \text{diag}(0.5, 0.5)$. Ellipses and peanuts both form circles and solutions to Eq. (2) reveal isotropic diffusion. Middle and bottom rows: anisotropic cases, $D = \text{diag}(0.75, 0.25)$ and $\text{diag}(0.9, 0.1)$, respectively. With increasing anisotropy the ellipses/peanuts become increasingly elongated/pinched. Solutions to (2) now show anisotropic spread, with equal density contours proportional to the anisotropy ellipse. Simulations of (2) are performed on the 2D domain of dimensions 10×10, with $\phi(\mathbf{x},t)$ represented through the colour-coded density map ($\phi = 0$, black; $\phi \geq 0.1$, white) and augmented by contours at $\phi = 0.001$ (dashed line) and $\phi = 0.01$ (solid). Numerical method described in Appendix B. (For interpretation of the references to color in this figure caption, the reader is referred to the web version of this article.)

these ideas in Section 5 to glioma invasion, using both artificial and real DTI datasets to illustrate the potential role of anisotropy on the invasive spread of tumours. We conclude with a brief discussion and description of future extensions.

2. Diffusion tensor imaging

2.1. Anisotropic diffusion and diffusion tensors

Anisotropic diffusion is typically expressed through the anisotropic diffusion equation:

$$c_t(\mathbf{x},t) = \nabla \cdot (D\nabla c(\mathbf{x},t)), \qquad (2)$$

where $D \in \mathbb{R}^{n \times n}$ is a given symmetric and positive definite matrix, or *diffusion tensor*. Example numerical solutions to (2) under various D are plotted in Fig. 2. The fundamental solution of (2) in n dimensions is given by

$$c(\mathbf{x},t) = \frac{1}{\sqrt{\det D(4\pi t)^n}} \exp\left(-\frac{1}{4t}\mathbf{x}^T D^{-1}\mathbf{x}\right).$$

The density $c(\mathbf{x},t)$ describes the probability density for finding a random walker (starting at location $\mathbf{0}$, time 0) at location $\mathbf{x}$, time t and forms an n-dimensional normal distribution with mean zero and variance–covariance matrix $= 2tD$. The *mean squared displacement in a given direction* $\theta \in \mathbb{S}^{n-1}$ (where $\mathbb{S}^{n-1}$ is the $(n-1)$-dimensional unit sphere) is $\sigma_\theta^2 = 2t\,\theta^T D\theta$ and the *apparent diffusion coefficient in direction* θ is defined as (see Basser, 2008):

$$ADC_\theta := \frac{\sigma_\theta^2}{2t} = \theta^T D\theta.$$

These formulae suggest two ways of visualising a diffusion tensor. First, the level sets of the probability density function $\phi(\mathbf{x},t)$ are given by

$$\mathbf{x}^T D^{-1} \mathbf{x} = \text{const.}, \tag{3}$$

which define n-dimensional ellipsoids, i.e. the areas of equal probability for finding the random walker are ellipsoids. For example, taking the diagonal matrix $D = \text{diag}(\lambda_1, \ldots, \lambda_n)$ with eigenvalues $\lambda_1 \geq \ldots \geq \lambda_n \geq 0$, Eq. (3) yields

$$\frac{x_1^2}{\lambda_1} + \cdots + \frac{x_n^2}{\lambda_n} = \text{const.},$$

which is an n-dimensional ellipsoid with semi-axes aligned along the coordinate directions and with their lengths proportional to $\sqrt{\lambda_1}, \cdots, \sqrt{\lambda_n}$. In Fig. 2 we plot examples of anisotropy ellipsoids (in 2D).

Second, the apparent diffusion coefficient ADC_θ in the specific direction θ defines a map

$$\mathbb{S}^{n-1} \rightarrow \mathbb{R}, \quad \theta \mapsto \theta^T D \theta,$$

and the graph of this map over $\mathbb{S}^{n-1}$ resembles a *peanut*. The peanut is aligned with directions of high diffusivity and pinched in directions of small diffusivity. Example peanuts are shown in Fig. 2.

These examples illustrate how distinct diffusion tensors generate ellipsoids and peanuts of varying shape, with their eigenvalues and eigenvectors determining their elongation and directionality, respectively. A variety of formulae based on the eigenvalues have been proposed to measure the anisotropy, two common ones being the ratio of anisotropy (RA) and fractional anisotropy (FA). Table 1 gives these measures for two and three dimensions. Fractional anisotropy is normalised to attain values in [0,1], with FA(D) = 0 corresponding to the isotropic case (e.g. $D = \text{diag}(1,1,1)$) and FA(D) = 1 denoting a completely anisotropic case (e.g. a degenerate scenario, $D = \text{diag}(1,0,0)$, with diffusion occurring in only one dimension). The anisotropy ratio can have values between 1 and ∞, where RA(D) = 1 corresponds to the isotropic case and RA(D) = ∞ is a degenerate case with at least one zero eigenvalue.

More detailed information about the shape of the diffusion tensor/ellipsoid can be obtained by computing the linear (a_l), planar (a_p) and spherical (a_s) indices (e.g. see Jbabdi et al., 2005). Assuming a (3D) diffusion tensor D with eigenvalues $\lambda_1 \geq \lambda_2 \geq \lambda_3$, these are defined as

$$a_l = \frac{\lambda_1 - \lambda_2}{\text{tr}}, \quad a_p = \frac{2(\lambda_2 - \lambda_3)}{\text{tr}}, \quad a_s = \frac{3\lambda_3}{\text{tr}},$$

where tr denotes the trace of D. These indices satisfy $a_l + a_p + a_s = 1$ and provide information on the shape of the corresponding diffusion ellipsoid: if $a_l \approx 1$ then the ellipsoid is "linear" shaped (like a long, thin cigar), if $a_p \approx 1$ it is disk shaped and if $a_s \approx 1$ it is spherical.

Table 1

Anisotropy measures in two and three dimensions. λ_i denote the eigenvalues of a diffusion tensor D in which $\lambda_1 > 0$ and (2D) $\lambda_1 \geq \lambda_2 \geq 0$, (3D) $\lambda_1 \geq \lambda_2 \geq \lambda_3 \geq 0$.

Measure		2D	3D
Ratio of anisotropy	(RA)	$\frac{\lambda_1}{\lambda_2}$	$\sup\left\{\frac{\lambda_1}{\lambda_2}, \frac{\lambda_1}{\lambda_3}\right\}$
Fractional anisotropy	(FA)	$\frac{|\lambda_1 - \lambda_2|}{\sqrt{\lambda_1^2 + \lambda_2^2}}$	$\frac{\sqrt{(\lambda_1 - \lambda_2)^2 + (\lambda_2 - \lambda_3)^2 + (\lambda_1 - \lambda_3)^2}}{\sqrt{2(\lambda_1^2 + \lambda_2^2 + \lambda_3^2)}}$

2.2. DTI

Magnetic resonance (MR) and DTI measurements are based on the magnetisation of water molecule dipoles in tissue. In MR measurements a strong external magnetic field aligns the spins in a plane perpendicular to the magnetic field and the relaxation to the original state is measured by a reduction in the overall magnetic moment (attenuation). Through applying specific excitation–relaxation sequences under spatial gradients of the magnetic fields it is possible to measure the diffusion tensor for the water molecules (see Basser, 2008; Rohmer and Gullberg, 2006). This water diffusion tensor, which from here on we denote by D_{TI}, is a symmetric 3×3 matrix with six independent parameters, thus requiring at least six independent measurements. Typically, measurements in more than six directions are obtained, to reduce the measurement error.

The capacity of DTI to determine the anisotropic diffusion tensors of water molecules provides the means to identify and visualise aligned structures, for example the white matter neural tracts of the CNS. Enhanced diffusion in a specific direction indicates greater freedom of movement and the local alignment of structures. Scanning the full CNS provides a set of values for $D_{TI}(\mathbf{x})$, where $\mathbf{x}$ represents the spatial coordinates for locations at which the diffusion tensor is measured, and connecting the anisotropy at one point with that at its neighbours provides a basic algorithm for computing the arrangement and alignment of fibres, a method known as tractography (Basser, 2008). We do not specifically consider tractography here, rather we will directly utilise the raw diffusion tensor data generated from DTI to inform our modelling.

3. Cell movement in anisotropic environments

The capacity of glioma cells to align with the neural fibre tracts suggests a transport equation approach in which a cell population is parametrised by time, space and velocity. An advantage is that logical rules can be proposed for the direction/velocity of cell movement according to the local environment, with a clear path for connecting measurable data (environment structure, cell speeds and turning distributions) to model inputs.

While this model operates at the *mesoscopic* scale of individual cell movement, our eventual scale of interest (glioma spread) is *macroscopic* and we will use parabolic scaling methods to generate a form of anisotropic diffusion equation, similar but distinct to that in (1). We note that the basic model was first derived in Hillen (2006) in the context of contact guided migration along collagen fibres and further analysed in Painter (2009), Hillen et al. (2010), and Hillen and Painter (2013).

We assume that the cells are represented by their density $p(t,\mathbf{x},\mathbf{v})$, where t denotes time, $\mathbf{x}$ is the position in space and $\mathbf{v}$ is the cell velocity. Generally we can expect the domain in which cells move to be a three-dimensional bounded domain—the CNS in the context of glioma invasion—however, here we simply state $\mathbf{x} \in \mathbb{R}^n$ for $n \leq 3$. We assume a closed set of cell velocities $\mathbf{v} \in V = [s_1, s_2] \times \mathbb{S}^{n-1}$, where the minimum ($s_1$) and maximum ($s_2$) cell speeds obey $0 \leq s_1 \leq s_2 < \infty$.

The time evolution for $p(t,\mathbf{x},\mathbf{v})$ is then described by the *transport equation*:

$$p_t(t,\mathbf{x},\mathbf{v}) + \mathbf{v} \cdot \nabla p(t,\mathbf{x},\mathbf{v}) = \mathcal{L}p(t,\mathbf{x},\mathbf{v}), \tag{4}$$

where $\mathcal{L}$ is the *turning operator* that describes the velocity changes of the individual cells. The above states that migration can be described as a sequence of "running" and "turning" events, with the operator $\mathcal{L}$ determining the frequency of a turn and the new

velocity choice. More precisely, we set

$$\mathcal{L}p(t,\mathbf{x},\mathbf{v}) = -\mu p(t,\mathbf{x},\mathbf{v}) + \mu \int_V q(t,\mathbf{x},\mathbf{v},\mathbf{v}')p(t,\mathbf{x},\mathbf{v}')\,d\mathbf{v}', \tag{5}$$

where the two right hand side terms, respectively, describe turning away and into velocity $\mathbf{v}$. The parameter μ denotes the *turning rate* ($1/\mu$ is the *mean run time*). The function $q(t,\mathbf{x},\mathbf{v},\mathbf{v}')$ describes the *cell turning distribution*: the distribution for the probability of a cell choosing new velocity $\mathbf{v}$ given previous velocity $\mathbf{v}'$. Note that mass conservation requires

$$\int_V q(t,\mathbf{x},\mathbf{v},\mathbf{v}')\,d\mathbf{v}' = 1. \tag{6}$$

The relevant model parameters of (4) and (5) are the turning rate μ and the integral kernel q for the turning angle distribution. For the turning rate we assume that it is constant ($\mu = $ const.) and hence we assume a mean turning time of $1/\mu$. To link DTI data into our model we will (Section 4) take a direct route by assuming the turning distribution depends on the anisotropy indicated by the diffusion tensors from DTI: effectively, the links between a given diffusion tensor and the local orientation of fibre tracts and the cell response to that architecture will be compressed into a single statement. Setting the model requires assumptions for the cell turning response to their surrounding environment and, in the absence of precise data, we make a number of simplifying assumptions that present the model in a clear manner and facilitate its mathematical treatment. Additional data will allow us to revise these assumptions at a later stage. Note that in the following we will specifically use "fibres" to describe the aligned underlying structure, although we acknowledge that other aligned structures, such as blood capillaries, can also contribute to guided movement.

We assume that the new velocity $\mathbf{v}$ is independent of the prior velocity $\mathbf{v}' : q(t,\mathbf{x},\mathbf{v},\mathbf{v}') = q(t,\mathbf{x},\mathbf{v})$. Thus, no persistence of migration is built explicitly into the cell turning distribution, inertia is neglected and directional guidance from the underlying fibre structure is assumed to be the dominating effect on cell turning. This convenient assumption allows us to immediately rewrite Eqs. (4) and (5) in the simpler form:

$$p_t(t,\mathbf{x},\mathbf{v}) + \mathbf{v}\cdot\nabla p(t,\mathbf{x},\mathbf{v}) = -\mu p(t,\mathbf{x},\mathbf{v}) + \mu q(t,\mathbf{x},\mathbf{v})c(t,\mathbf{x}), \tag{7}$$

where we have defined the *macroscopic cell density*

$$c(t,\mathbf{x}) = \int_V p(t,\mathbf{x},\mathbf{v})\,d\mathbf{v}.$$

We further assume that the speed of the cells is constant and independent of the underlying structure, i.e. we choose for simplicity $V = s \times \mathbb{S}^{n-1}$ where s is the average cell speed. It is straightforward to generalise this model for varying speed (e.g. see Hillen, 2006) but we see no necessity to include this aspect at this stage. The constant speed assumption is certainly a simplification and ignores the hypothesis that cells can switch between a stationary, proliferative and migratory, nonproliferative phenotype ("go-or-grow", e.g. see Pham et al., 2012 and references therein): speed here would therefore most appropriately refer to a population-averaged rate, also including nonmigratory cells. An expansion of the framework to explicitly model the impact of a dichotomy between proliferation and migration will be considered in future extensions.

With cell velocity parametrised for $\mathbf{v} \in V$, we can write

$$q(t,\mathbf{x},\mathbf{v}) = \frac{\hat{q}(t,\mathbf{x},\theta)}{s^{n-1}}. \tag{8}$$

The new cell turning distribution $\hat{q}$ now describes the probability of turning into a direction θ, with the property

$$\int_{\mathbb{S}^{n-1}} \hat{q}(t,\mathbf{x},\theta)\,d\theta = 1.$$

Assuming that cells tend to migrate along the orientated neural fibre tracts, for example, Giese et al. (1996, 2003); Clatz et al. (2005); Bondiau et al. (2008); Konukoglu et al. (2010); and Jbabdi et al. (2005), and that the alignment of the latter is reflected through DTI derived datasets, we will later use the measured DTI tensors to define this turning kernel $\hat{q}(t,x,\theta)$. We will also assume that the geometry of the brain is unchanged on the time-scale of the model, i.e. $\hat{q} = \hat{q}(x,\theta)$. Again, while it is straightforward to consider evolving geometries and hence time-dependent $\hat{q}$ (e.g. see Hillen, 2006) we currently omit this.

We finally note that the symmetric properties of DTI diffusion tensors imply that the kernel $\hat{q}$ must also be symmetric as well, i.e.

$$\hat{q}(\mathbf{x},-\theta) = \hat{q}(\mathbf{x},\theta) \quad \text{for all } \theta \in \mathbb{S}^{n-1}. \tag{9}$$

The above symmetry essentially imposes that cells do not choose a specific direction: an "up" or "down" direction will be chosen with equal probability. The exact form of $\hat{q}$ requires some further insights into the movement of cells and their statistics and will be discussed in Section 4.

One further observation is that rather than taking the direct route of stating $\hat{q}$ from the DTI data, we could first model the tissue architecture implied by DTI and then specify the cell turning distribution according to the tissue network. For example, by defining a fibre distribution $m(t,x,\theta)$ which gives the distribution of fibre directions at time t and location x, then a simple and logical model for contact guidance would be $\hat{q}(t,\theta) = m(t,\mathbf{x},\theta)$, i.e. a cell directly chooses its direction according to the local fibre distribution. In fact, this approach was originally taken in Hillen (2006) and Painter (2009). For the current purposes, however, this is overly ornate and rather we directly postulate the cell turning distribution $\hat{q}$ according to information encoded in the DTI data, and only implicitly assume a fibre structure of the brain.

Summarising Eq. (7) describes a process of oriented cell migration in which cells move with a constant average speed s and turn at a rate μ. The cell turning distribution $\hat{q}$ will translate alignment of the fibres as measured through DTI to contact guided movement of cells. While simple in nature, we note that the framework can be extended, for example providing an explicit description of an evolving CNS architecture.

3.1. Parabolic scaling to a macroscopic model

The transport model (7) is a mesoscopic scale description of migration: although continuous, it is an individual-level description of movement and parametrised accordingly. Thus, within the transport model, length scales will be of the order of microns, with time scales on the order of minutes. Glioma growth, on the other hand, where tumours grow over months to years and extend over centimetres, is a macroscopic process and we now summarise the bridging of these scales.

Scalings can be motivated in a variety of ways, for example by considering quick turning and fast cell speed relative to the time frame of observation, or scaling space and time from the microscopic to the macroscopic: see Hillen and Painter (2013) for a detailed discussion. As an example, even though a cell may turn infrequently (on a timescale of minutes), over the course of glioma growth a large number of reorientations are likely to take place. Working within this much longer timescale allows the introduction of small parameters which can be exploited through formal expansions. Specifically, under the symmetry constraint (9), we can apply the parabolic scaling (see Hillen and Painter, 2013 for the details) and derive the following leading order approximation for the macroscopic cell density $c(t,\mathbf{x})$:

$$c_t(t,\mathbf{x}) = \nabla\nabla(D_C(\mathbf{x})c(t,\mathbf{x})), \tag{10}$$

with *macroscopic diffusion tensor*

$$D_C(\mathbf{x}) = \frac{s^2}{\mu} \int_{\mathbb{S}^{n-1}} \theta\theta^T \hat{q}(\mathbf{x},\theta) \, d\theta. \tag{11}$$

We use the index C on D_C as an indication of the cell-diffusion tensor, which is our primary application at this point. Superficially similar to the standard anisotropic diffusion equation (2), we note the distinct positioning of the diffusion tensor in (10). This difference can have far-reaching consequences, as Eq. (10) does not satisfy a maximum principle and it can lead to aggregations and even blow-up, as shown in Hillen et al. (2013). We further remark that D_C is positive-definite when $\hat{q}(\mathbf{x},\cdot)$ is a regular probability distribution and, in this case, Eq. (10) will be uniformly parabolic with all the existence and uniqueness theorems of parabolic equations applying (e.g. Evans, 1998).

4. Connecting DTI and cell diffusion tensors

Above we have explained the capacity for DTI to encode information on the anisotropy of white matter in the CNS and derived both mesoscopic and macroscopic models for cell migration/invasion in response to this anisotropy. In this section, we propose the mapping of the DTI dataset to the cell turning distribution $\hat{q}$ and, via (11), to a cell diffusion tensor $D_C(x)$ for the macroscopic model (10).

First we consider some trivial scaling arguments to aid our intuition. We neglect the physical mechanisms that attach and orient migrating glioma cells along the myelinated fibre tracts and simply reflect on the restricted diffusion of molecule and cell sized objects amongst them. Water molecules are comparatively tiny and we would still expect a degree of diffusion into directions orthogonal to the fibre tract orientation. A cell-sized object, on the other hand, would find itself in a tightly restricted space with limited freedom of movement. Consequently, we expect it would experience greater anisotropy than a molecule and the straight identification $D_C \equiv D_{TI}$ would be rather naive, stating cells move exactly as water molecules.

To develop a more realistic relation between D_{TI} and D_C we use the above transport equation framework. We infer the geometry on the neural fibres from the DTI measurements, stating a suitable turning distribution $\hat{q}$ from which we compute the cell diffusion tensor D_C as given in (11).

4.1. Using the peanut of D_{TI}

Earlier we noted that the apparent diffusion coefficient in a given direction, $ADC_\theta = \theta^T D_{TI}\theta$, is an important indicator of anisotropy: a very simple assumption is to assume cell turning is directly correlated. While we later find that this is an inappropriate choice, we quickly discuss this case as an illustration of the need for due consideration of $\hat{q}$. Thus we take the cell turning into angle θ to be

$$\hat{q}(\mathbf{x},\theta) := \frac{n}{|\mathbb{S}^{n-1}| \operatorname{tr} D_{TI}(\mathbf{x})} \theta^T D_{TI}(\mathbf{x})\theta. \tag{12}$$

In the above, $\operatorname{tr} D_{TI}$ denotes the trace of D_{TI} and the term in front of ADC_θ is the normalisation coefficient. Substituting (12) into (11) we compute (see Lemma 1 in Appendix A) the following macroscopic cell diffusion tensor:

$$D_C(\mathbf{x}) = \frac{s^2}{\mu(2+n)} \left(\mathbb{I} + \frac{2}{\operatorname{tr} D_{TI}(\mathbf{x})} D_{TI}(\mathbf{x}) \right), \tag{13}$$

where $\mathbb{I}$ denotes the identity matrix. The above reveals a direct relationship between the DTI diffusion tensor D_{TI} and the macroscopic diffusion tensor D_C, the latter consisting of an isotropic

component (the $\mathbb{I}$-term) and a term proportional to D_{TI}. We observe that D_{TI} and D_C have equivalent eigenvectors, indicating that their corresponding ellipsoids are parallel and cell diffusion is enhanced in the same direction as the DTI dataset.

We further note that the isotropic component of D_C is completely independent of D_{TI}, indicating that there will always be an element of isotropic cell diffusion, even when D_{TI} itself is completely anisotropic. Computing the anisotropies of D_{TI} and D_C using the measures FA and RA from Table 1, we find (see Lemma 2 in Appendix A) that the anisotropy of the cell tensor is bounded and always lower than that of D_{TI}. In Lemma 2 of Appendix A we also compute the linear, planar, and spherical indices of D_C and find that D_C given by (13) is more spherical than D_{TI}. This counteracts both our intuitive expectations and the findings (by clinical matching) of Jbabdi et al. (2005), suggesting our first choice is inappropriate.

4.2. Using the eigenvectors and fractional anisotropy of D_{TI}

Our next approach is to follow a natural path in which cell turning takes the form of a normal distribution on the unit sphere, called a *von Mises or Fisher distribution* (Mardia and Jupp, 2000). We briefly note that $D_{TI}(\mathbf{x})$ (assumed positive definite and symmetric) can be represented as

$$D_{TI}(\mathbf{x}) = \sum_{i=1}^{n} \lambda_i(\mathbf{x})\varphi_i(\mathbf{x})\varphi_i(\mathbf{x})^T, \tag{14}$$

for eigenvalues $\lambda_1 \geq \ldots \geq \lambda_n \geq 0$ and their corresponding (orthogonal and normalised) eigenvectors $\varphi_1(\mathbf{x}) \ldots \varphi_n(\mathbf{x})$. $\varphi_1(\mathbf{x})$ indicates the axis of dominating anisotropy and the sizes of the eigenvalues determines the degree of anisotropy. We exploit this information to determine $\hat{q}$, aiming for a transparent connection that incorporates the main idea.

4.2.1. Two-dimensional case

To facilitate the presentation our main attention is focused on a two-dimensional slice of tissue, although we note that the results can be extended to three dimensions (see below). In two dimensions, the water diffusion tensor is given by (14) with eigenvalues $\lambda_1(\mathbf{x}) \geq \lambda_2(\mathbf{x}) \geq 0$ and eigenvectors $\varphi_1(x)$, $\varphi_2(x)$.

We begin by introducing the von Mises distribution:

$$P(\theta) = N_2(k)e^{k\gamma\cdot\theta}, \tag{15}$$

where, in 2D, $\theta = (\cos\alpha, \sin\alpha)$ for $\alpha \in [0,2\pi)$. In the above, $\gamma \in \mathbb{S}^1$ and $k \in \mathbb{R}$, respectively, define the *dominating direction* and *parameter of concentration*. The coefficient

$$N_2(k) = \frac{1}{2\pi I_0(k)}$$

acts as a normalisation coefficient, where we use I_j to denote the modified Bessel function of first kind of order j. The distribution (15) generates a single peak in direction γ, increasingly concentrated with k, and defines a normal distribution on a circle. Extended to bimodal form,

$$P_B(\theta) = N_2(k)\frac{e^{k\gamma\cdot\theta} + e^{-k\gamma\cdot\theta}}{2},$$

we obtain two equal maxima in the directions γ and $-\gamma$, respectively.

Our proposition is to specify $\hat{q}$ according to the above, using the measures of D_{TI} to determine k and γ, respectively. A natural choice is to assume that turning is concentrated in the direction of the dominating D_{TI} anisotropy and we take

$$\hat{q}(\mathbf{x},\theta) = \frac{\delta}{2\pi} + (1-\delta)N_2(k(\mathbf{x}))\frac{e^{k(\mathbf{x})\varphi_1(\mathbf{x})\cdot\theta} + e^{-k(\mathbf{x})\varphi_1(\mathbf{x})\cdot\theta}}{2}, \tag{16}$$
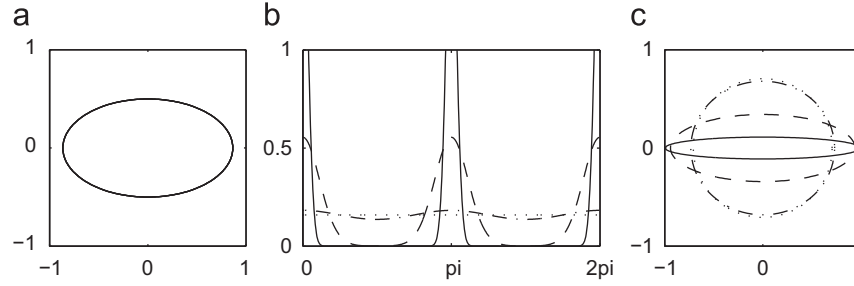
Fig. 3. Converting D_{TI} to D_C through (16)–(18). (a) We set $D_{TI} = \text{diag}(0.75, 0.25)$ and plot the anisotropy ellipse. (b) Calculation of $\hat{q}$ from (16) and (17) with $\delta = 0$ and $\kappa = 0$ (dotted line), $\kappa = 1$ (dot-dash), $\kappa = 10$ (dashed) and $\kappa = 100$ (solid). For $\kappa = 0$, anisotropy is ignored and the corresponding $\hat{q}$ is uniform. For positive κ cells become more likely to turn into directions corresponding to the anisotropy of D_{TI}, with turning becoming increasingly restricted as κ increases. Here we plot $\hat{q}$ as a function of $\theta = (\cos \alpha, \sin \alpha)$ for $\alpha \in [0, 2\pi)$. (c) Corresponding anisotropy in D_C is highly tunable. In all calculations, we set $s^2/\mu = 2$.

where the constant parameter $\delta \in [0,1]$ specifies an inherent degree of randomised turning. The function $k(\mathbf{x})$ describes the level of concentration around the dominant direction: intuitively, cells should become increasingly aligned with greater anisotropy of the environment (i.e. of D_{TI}) and hence it is chosen to be proportional to the fractional anisotropy (Table 1):

$$k(\mathbf{x}) := \kappa \, \text{FA}(D_{TI}(\mathbf{x})), \tag{17}$$

where $\kappa \geq 0$ is a proportionality constant which denotes the sensitivity of the cells to the directional information in the environment. In the isotropic case, $\text{FA}(D) = k(\mathbf{x}) = 0$ and the von Mises distribution becomes a uniform distribution. For the maximum anisotropy of $\text{FA} = 1$ we have $k(\mathbf{x}) = \kappa$.

Computing the diffusion tensor D_C from (11) using (16) involves computing the second moment of a bimodal von Mises distribution. This was done in Hillen and Painter (2013) and here we simply cite the result:

$$D_C(\mathbf{x}) = \frac{s^2}{2\mu} \left(\left(\delta + (1-\delta) \left(1 - \frac{I_2(k(\mathbf{x}))}{I_0(k(\mathbf{x}))} \right) \right) \mathbb{I} \right.$$
$$\left. + 2(1-\delta) \frac{I_2(k(\mathbf{x}))}{I_0(k(\mathbf{x}))} \varphi_1(\mathbf{x}) \varphi_1(\mathbf{x})^T \right). \tag{18}$$

Once again, D_C is split into isotropic (the $\mathbb{I}$ term) and anisotropic components, with the anisotropy pointing in the directions $\pm \varphi_1(\mathbf{x})$. The relative sizes of these terms are determined by δ and the function $k(\mathbf{x})$.

To evaluate the utility of (18), we note that $I_2(k)/I_0(k) = 0$ when $k = 0$ and $I_2(k)/I_0(k) \to 1$ as $k \to \infty$. Hence, for either an isotropic D_{TI} ($\lambda_1 = \lambda_2$) or a cell population that does not respond to environmental anisotropy ($\kappa = 0$), we have $k = 0$ in (17) and D_C is correspondingly isotropic. As we move towards a degenerate D_{TI} ($\lambda_1 > 0$, $\lambda_2 \to 0$) we have $k \to \kappa$. Thus, choosing cell turning according to (16) and (17) permits enhanced anisotropy, which is only bounded by the choices of δ, κ (see Lemma 3 in Appendix A). In Fig. 3(a)–(c) we illustrate the translation between D_{TI} and D_C as described above, demonstrating how the parameter κ tightens or loosens the range of cell turning in response to the anisotropy in D_{TI}, with a corresponding increase or decrease in the anisotropy of D_C.

4.2.2. Three-dimensional case

We do not consider in detail the three-dimensional situation, however, we do briefly present a natural extension of the above and the corresponding translation to a 3D tumour diffusion tensor. We employ the 3D version of the von Mises–Fisher distribution (Mardia and Jupp, 2000) and again combine it with a uniform distribution, with parameter $\delta \in [0,1]$ reflecting the predominance of random over oriented turning. The distribution

for turning into direction $\theta \in \mathbb{S}^2$ is proposed as

$$\hat{q}(\mathbf{x}, \theta) = \frac{\delta}{4\pi} + (1-\delta) \frac{k(\mathbf{x})}{4\pi \sinh(k(\mathbf{x}))} \cosh(k(\mathbf{x}) \varphi_1(\mathbf{x}) \cdot \theta). \tag{19}$$

Once again, $\varphi_1(\mathbf{x}) \in \mathbb{S}^2$ denotes the dominating direction of anisotropy in D_{TI} at a given point and the concentration parameter $k(\mathbf{x})$ can be taken proportional to the fractional anisotropy.

In this case the tumour diffusion tensor of $\hat{q}(\mathbf{x}, \theta)$ is given as (see Mardia and Jupp, 2000; Hillen and Painter, 2013)

$$D_C(\mathbf{x}) = \frac{s^2}{3\mu} \left[\left(\delta + (1-\delta) \left(\frac{\coth k}{k} - \frac{1}{k^2} \right) \right) \mathbb{I} \right.$$
$$\left. + (1-\delta) \left(1 - \frac{3 \coth k}{k} + \frac{3}{k^2} \right) \varphi_1 \varphi_1^T \right]. \tag{20}$$

Note that we have omitted the $\mathbf{x}$ dependence in the RHS functions k and φ_1. The derivation of this formula is quite technical and exceeds the intentions of the present paper and will be presented in Hillen and Painter (2013).

5. Simulating glioma invasion

We directly apply the above analysis in a simple two-dimensional model for glioma growth. We stress that the results are currently illustrative and the model remains intentionally simple to focus on how imaging data can be mapped to investigate invasive spread. Specifically, we assume that the tumour to be dominated by a homogeneous cell type, defining $c(\mathbf{x}, t)$ to be the density of cancerous cells at position $\mathbf{x} \in \Omega$. Ω defines a bounded region that marks the extent of the central nervous system (CNS). We neglect all tumour–host interactions beyond the directional spread of cells along the alignment inferred from DTI data and simply augment the macroscopic model (10) with a proliferation term, $f(c)$:

$$c_t = \nabla \nabla (D_C(\mathbf{x}) c) + f(c), \tag{21}$$

where $D_C(\mathbf{x})$ defines the macroscopic glioma cell diffusion tensor. For $f(c)$ we employ the standard logistic form $f(c) = rc(1 - c/c_m)$, where r defines the cell proliferation rate and c_m describes a tissue "carrying capacity". While undoubtedly naive, this facilitates comparison with standard results for the classical Fisher equation: in 1D with $D_C(x) = D$ (constant) we expect travelling waves with wavespeed $2\sqrt{rD}$.

While three-dimensional studies are certainly feasible (at increased computational expense), a two-dimensional analysis, representing a slice of tissue, suffices for the present purposes. We therefore set $\mathbf{x} = (x, y) \in \Omega \subset \mathbb{R}^2$, assume zero flux (no gain/loss) conditions on the boundary $\partial \Omega$ and a given set of initial conditions $c(x, y, 0) = c_0(x, y)$. The numerical method is described in Appendix B.
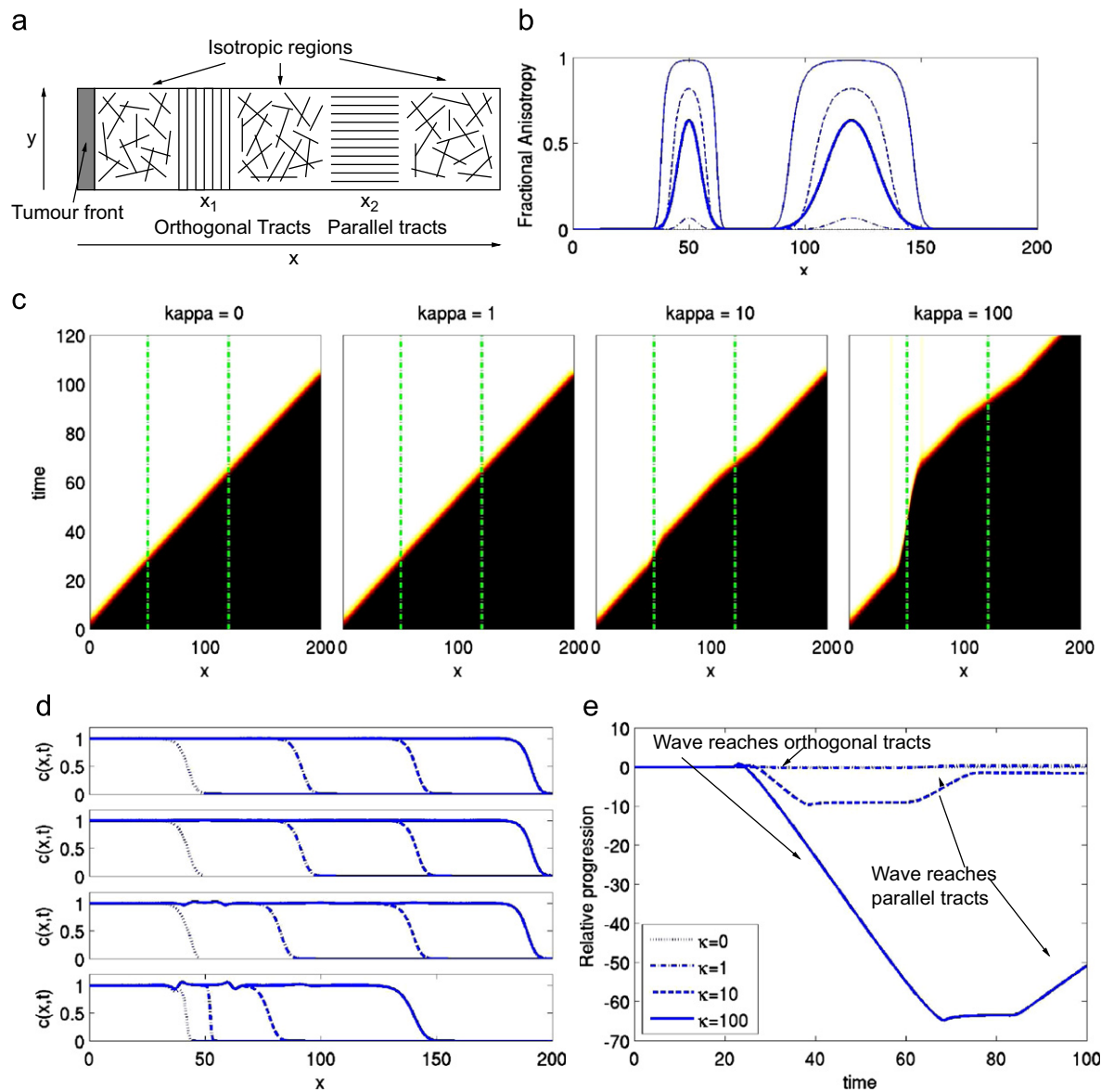
Fig. 4. (a) Schematic showing the initial set-up for a quasi-1D scenario. (b) Comparison of fractional anisotropies for D_{TI} (thick solid line) and D_C under $\kappa = 0$ (dotted), 1 (dot-dash), 10 (dashed), 100 (thin solid). (c) Space–time maps show the evolving cell density: colourmap scales from black ($c(x,t) = 0$) to white ($c(x,t) \geq 1$) and vertical dash lines indicate the centres of the aligned regions. Left to right figures show the results for $\kappa = 0, 1, 10$ and 100. For $\kappa = 0$ the interface is a straight line, corresponding to a constant invasion rate. For $\kappa > 0$ the interface becomes jagged, indicating a variable rate of invasion with position. (d) Profiles showing cell densities at $t = 25$ (dotted), 50 (dot-dash), 75 (dashed) and 100 (solid). Top to bottom panels plot the cell density profiles for $\kappa = 0, 1, 10, 100$. Note the nonuniform cell density profiles when $\kappa > 0$. (e) Relative progression of the wavefront. For each simulation we track the position $x^*(t)$ such that $c(x^*,t) = c_m/2$. Simulations solve Eq. (21) with D_C obtained from D_{TI} (defined in the text) through (16)–(18) for $\delta = 0$, $s^2/\mu = 2$ and varying κ. Other parameters are set at $r = c_m = 1$, $L_x = 200$ and $L_y = 5$. Numerical method as described in Appendix B, with $\Delta_x = \Delta_y = 0.1$ and $\Delta t = 10^{-4}$.

At this point we also note the phenomenological model previously proposed by Jbabdi et al. (2005), a natural point for comparison with (21):

$$c_t(t,\mathbf{x}) = \nabla(D_C(\mathbf{x})\nabla c(t,\mathbf{x})) + f(c), \tag{22}$$

where $D_C(\mathbf{x})$ also represents a diffusion tensor determined according to DTI data. While similar in nature, we remark on two key differences: (1) the model here, Eq. (21), has been derived from an explicit description of cell movement, with the macroscopic parameters (i.e. the macroscopic diffusion tensor) directly derived from the microscopic inputs such as cell speeds and cell turning distributions; (2) the distinct position of the diffusion tensor in (21) gives rise to additional advective-type terms, the impact of which will be demonstrated below.

5.1. Artificial datasets

5.1.1. Case (i): Quasi-one-dimensional scenario

We first consider a quasi-one-dimensional scenario in which initial cell densities and DTI data only vary along the x-axis of a rectangular strip of tissue $\Omega = [0,L_x] \times [0,L_y]$ with zero-flux boundary conditions. Initially we place the tumour front at the edge of the strip, setting $c_0(x,y) = 0.1e^{-x^2}$, and refer to Fig. 4(a) for a schematic of the initial configuration. We propose that the synthetic dataset D_{TI} varies along the x-axis according to

$$D_{TI}(x) = \begin{pmatrix} 0.5 - d(x) & 0 \\ 0 & 0.5 + d(x) \end{pmatrix}, \tag{23}$$
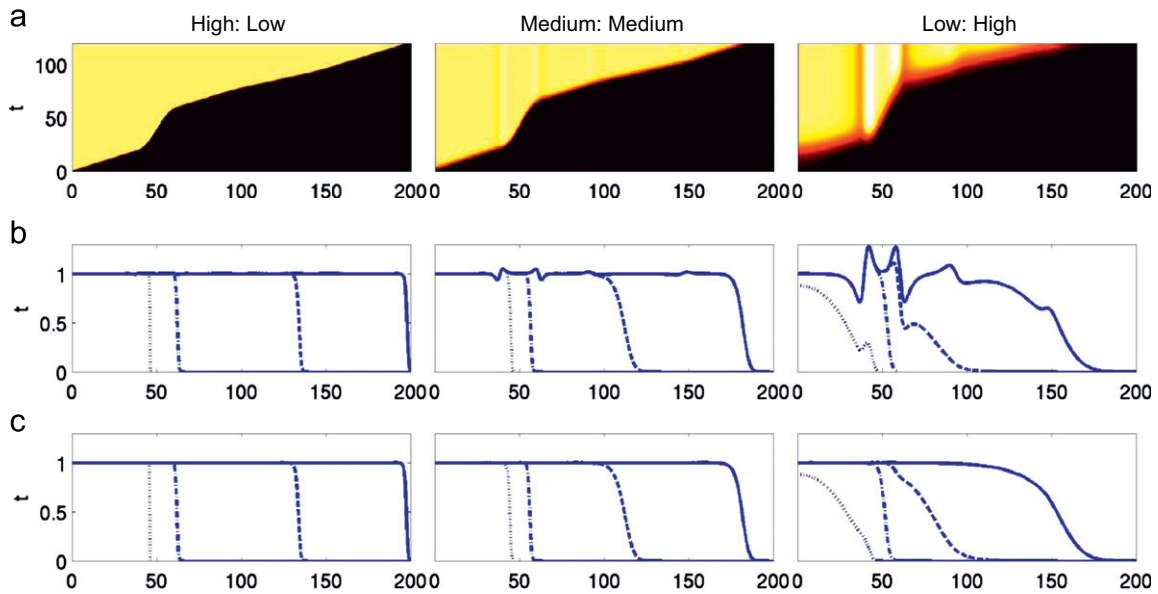
Fig. 5. Heterogeneity of the wave profile for invasion in anisotropic environments under a varying relative strength of motility:proliferation terms. (a) Space–time maps plotting the cell density: black, $c(x,t) = 0$; white, $c(x,t) \geq 1$. From left to right we consider a high:low-, medium:medium- and low:high-proliferative:motility ratio. (b) Corresponding plots showing the variation in cell density profiles. In each panel we plot the wave profile for the same three tumour classes at $t = 25,50,75$ and 100. Moving from high:low to low:high proliferation:motility generates an increasingly diffuse and (spatially) heterogeneous tumour. (c) For comparison, we show the corresponding simulations for model (22) using the same parameters as in (b). We clearly see the homogeneous distribution in the wake of the invasion front. In all simulations we choose D_C calculated from (16) to (18) with $\delta = 0.1$, $\kappa = 100$ and D_{TI} as for Fig. 4. The different phenotypes were modelled by setting: $s^2/\mu = 0.1$, $r = 5$ (high:low); $s^2/\mu = 0.5$, $r = 1$ (medium:medium); $s^2/\mu = 2.5$, $r = 0.2$ (low:high). Other parameters and numerical details as in Fig. 4.

where $d(x) \in [-0.5,0.5]$ for all x. The above defines a dataset in which the dominating anisotropy of the fibre tracts is either orthogonal (for $d(x) > 0$) or parallel (for $d(x) < 0$) to the x-axis: $d(x) > 0$ and $d(x) < 0$ therefore corresponds to either decreased or increased rates of diffusion along the x-axis (reversed along the y-axis). Here we explicitly set $d(x) = 0.25(e^{-0.025(x-50)^2} - e^{-0.005(x-120)^2})$, defining a tissue with regions of orthogonal and parallel tracts centered about $x = 50$ and $x = 120$, respectively, in an otherwise isotropic field. Taking advantage of the quasi-one-dimensional set-up, we ignore the (uniform) data in the y-direction and plot the variation with the x-axis only in Fig. 4.

We first illustrate the translation between D_{TI} and D_C through comparing their fractional anisotropies, exploiting (16)–(18) to connect DTI data to cell turning. As expected we observe that anisotropy of D_C is highly tunable, Fig. 4(b), lower or above that of D_{TI} according to the size of κ. Note that for $\kappa = 0$, the fractional anisotropy is 0.

We proceed to explore the impact of an anisotropic environment on the invasive spread of a cancer population in which cells have differing capability to align through simulating (21) under varying κ. In the "control" scenario ($\kappa = 0$), any environmental anisotropy is ignored by cells: the model (21) effectively reduces to a Fisher equation and invasion occurs in the form of a travelling wave with a constant rate of invasion, given by $2\sqrt{rs^2/2\mu}$. Increasing κ from zero introduces the impact from environmental anisotropy on cell turning, with consequent repercussions on the rate and form of invasion (Fig. 4(c)–(d)). As the invasive front moves into the region of orthogonally aligned fibre tracts, turning into this orientation acts to retard progression of the wave. On the other hand, a region of parallel fibre tracts acts as a cellular highway and accelerates the wavefront. Increases in κ enhances the impact of anisotropy on cell turning, with correspondingly greater slowing or acceleration of the wavefront in anisotropic regions. To illustrate this we track the position of the wavefront (relative to the control case) as a function of time (Fig. 4(e)): invasion becomes increasingly delayed with the size of κ as the front enters the orthogonal tract region, but recovers ground on reaching the parallel tracts.

The environment is therefore a significant factor in altering the rate of invasion. Further, it can also impact on the spatial cell density that emerges behind the wavefront, specifically at the interfaces between regions of varying anisotropy. Cell density profiles in Fig. 4(d) reveal an emerging pattern of troughs and peaks in cell density, enhanced under increasing κ. To investigate this phenomenon further, we explore the extent to which the cell density varies for three hypothetical tumour classes: high proliferation/low motility-, medium/medium- and low/high-phenotypes. Specifically, we compare the tumour profile as the relative ratio of diffusive to proliferative terms is altered. Note that these terms are varied such that invasion would occur at the same rate (i.e. with the same travelling wavespeed) in an isotropic environment.

Simulation results are plotted in Fig. 5. For a high proliferation/ low motility phenotype, we observe a compact tumour front with the invasive rate varying according to the local anisotropy. Little spatial variation can be observed in the tumour cell density emerging behind the wave. As we progress towards a low proliferation/high motility phenotype, however, we observe increasing variation in the cell density profile. We note that this pattern arises due to the specific form of (21). Local maxima arise near the transition regions from random to aligned tissue and, in the extreme case of sudden transitions, sharp peaks and even singularities might form, as analysed in Hillen et al. (2013). In contrast, the phenomenological model of (22) predicts a similar rate of invasion at the cell front but a uniform cell density distribution following passage of the wave under the same form of $f(c)$ (Fig. 5(c)). For the model derived from the transport equation it is the additional advective-type terms in (21) that act to direct cell movement in regions of spatially varying anisotropy, aggregating cell populations accordingly.

5.1.2. Case (ii): Anisotropy in two-dimensional invasion

In the above we focused on a quasi-one-dimensional scenario, providing detailed insight on the capacity for environmental alignment to alter the rate and profile of an invading tumour.
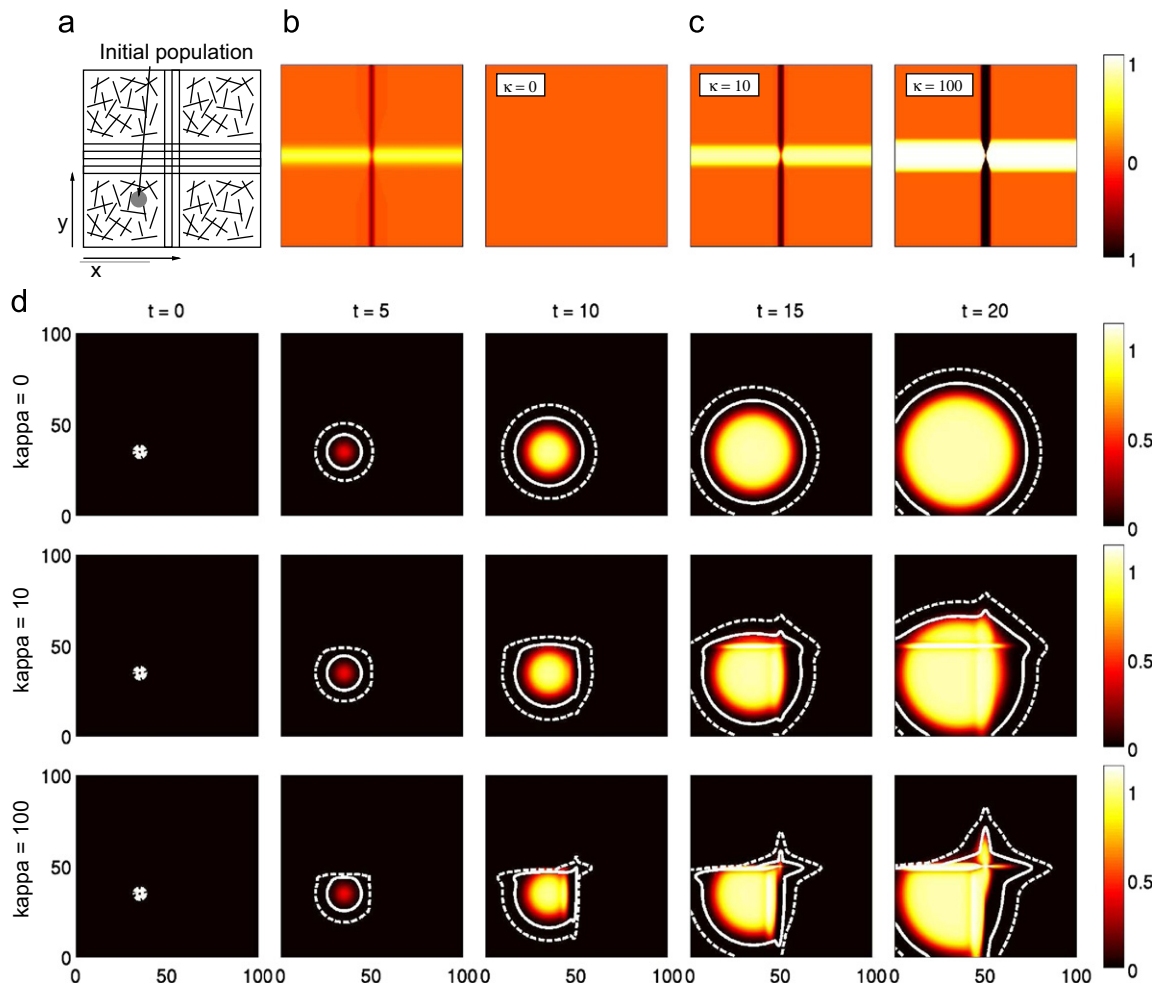
Fig. 6. Invasion for a synthetic 2D dataset. (a) Schematic showing the initial set-up and environment. (b-c) Comparison of fractional anisotropy in (b) D_{TI} and (c) D_C under various κ: colourmap indicates regions of vertical (black) and horizontal (white) alignment, with orange denoting isotropy. (f) Tumour growth evolution. In each row we show the evolving cell density for varying κ, plotting $c(x,y,t^*)$ at $t^* = 0$, 5, 10, 15, 20 as represented by the colourmap. All simulations solve Eq. (21) with D_C obtained from D_{TI} (described in the text) according to (16)–(18) with $\delta = 0.05$, $s = 1$, $\mu = 0.5$, $r = c_m = 1$ and varying κ. Numerical method as described in Appendix B with $\Delta_x = \Delta_y = 0.25$ and $\Delta t = 10^{-4}$. (For interpretation of the references to color in this figure caption, the reader is referred to the web version of this article.)

We next turn our attention to a similar two dimensional study. A schematic of the set-up employed in this section is illustrated in Fig. 6(a). Specifically, we consider a square slice $(x,y) \in \Omega = [0,100] \times [0,100]$ with zero-flux boundary conditions and populated with an initially circular cancer population centred on the point (35, 35):

$$c_0(x,y) = 0.1e^{-(x-35)^2}e^{-(y-35)^2}.$$

We begin by imposing a synthetic DTI dataset, considering a generally isotropic environment that contains a pair of orthogonal fibre tracts (of distinct widths) that run vertically and horizontally and cross at the centre, see Fig. 6(a). We therefore set our synthetic D_{TI} as

$$D_{TI}(x,y) = \begin{pmatrix} 0.5 - d(x,y) & 0 \\ 0 & 0.5 + d(x,y) \end{pmatrix}, \qquad (24)$$

where $d(x,y) \in [-0.5, 0.5]$ is given as

$$d(x,y) = 0.25e^{-0.05(x-50)^2} - 0.25e^{-0.5(y-50)^2}.$$

To illustrate the anisotropy in D_{TI} we plot the Fractional Anisotropy in Fig. 6(b), using a colour-coded map to illustrate the distinct directions of the anisotropy. Filtering D_{TI} to D_C in (21) via (16)–(18) under varying κ once again allows us to simulate populations with distinct capacities to align with the environment.

Simulations of (21) for $\kappa = 0$ are shown in Fig. 6(c): DTI/environmental anisotropy is ignored by the cells, growth is uniform and the tumour remains circular. Increasing κ, however, introduces an impact due to environmental anisotropy on the preferential spread of cells and the invasion becomes increasingly nonuniform: alignment of cells enhances invasion in the direction of the fibre tracts while retarding invasion in orthogonal directions, see Fig. 6(c) middle and bottom rows for examples with $\kappa = 10$ and 100. Consistent with the one-dimensional case, increasing κ magnifies this and we also observe an increasingly heterogeneous form for the cell density distribution in the wake of the wave, with ridges and valleys of cell density emerging in regions of highly variable anisotropy.

5.2. Genuine DTI datasets

Finally we address genuine imaging data, utilising software (DTIstudio, Jiang et al., 2006) and anonymous data available at http://www.mristudio.org/ to generate a DTI diffusion matrix D_{TI}. Fig. 7(a) demonstrates output from a typical dataset, plotting the spatially varying DTI anisotropy.

In line with previous sections our current focus is purely illustrative and we will restrict attention to a two-dimensional scenario: a fully predictive model would certainly require a three-dimensional analysis due to the potentially critical projection of
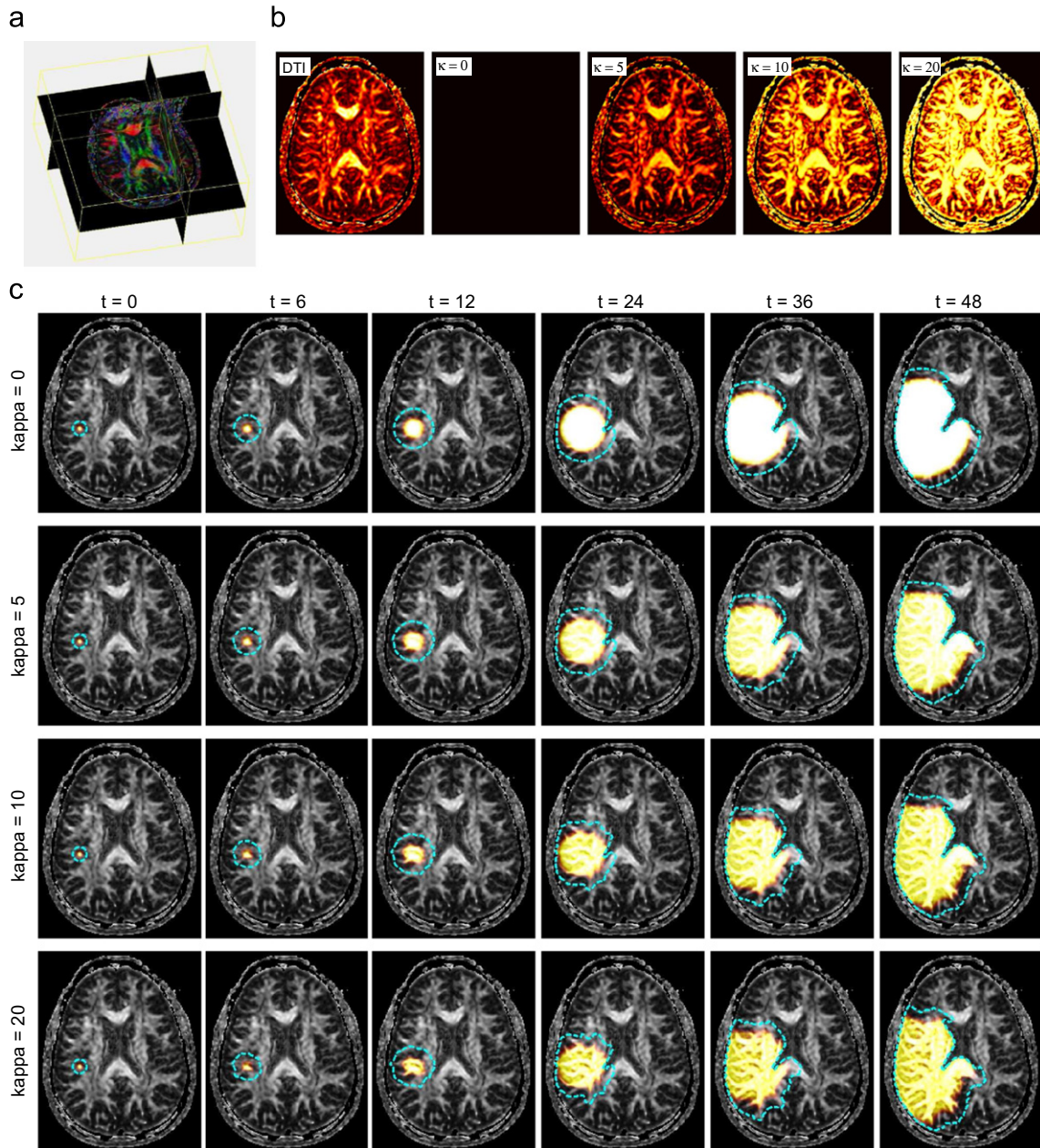
Fig. 7. Simulations of glioma growth using genuine DTI data. (a) 3D Anisotropy plot. (b) We use the 2D transverse slice shown for our simulations: its fractional anisotropy (black=low, isotropic; white=high, anisotropic) is shown for the D_{TI} dataset and the computed cell diffusion tensor D_C at the values of κ shown. (c) Evolution of glioma growth. Numerical solutions showing the solution of (21) at the times indicated (in months) for distinct values of κ. As we increase the strength with which cells align with the DTI anisotropy, we observe a more heterogeneous form of growth. Dashed light blue contour indicates $c(x,y) = 0.0001$. Parameters are set at $\delta = 0.05$, $s^2/mu = 1.25 \times 10^{-4}$ cm^2/day, $r = 0.025$/day, $c_m = 1$ and varying κ. Numerical method as described in Appendix B, with $\Delta_x = \Delta_y = 0.09375$ cm. (For interpretation of the references to color in this figure caption, the reader is referred to the web version of this article.)

fibre tracts into the ignored dimension. Here we consider the transverse (or horizontal) plane illustrated in Fig. 7(b) and discard diffusion tensor data in the vertical projection: in other words, we employ the 2×2 submatrix $D_{TI}(x,y)$ formed from the relevant rows and columns of the imaging data tensor matrix, with (x,y) denoting position in the plane.

From $D_{TI}(x,y)$ we extract the eigenvalues $\lambda_{1,2}(x,y)$ and corresponding (orthogonal and normalised) eigenvectors $\varphi_{1,2}(x,y)$. Note that anomalies in the data or noise introduced during processing can generate negative eigenvalues in the diffusion tensor matrix: these are removed through setting to zero. The imaging data stored in D_{TI} is then translated to a cell diffusion tensor matrix using Eqs. (16)–(18): see Fig. 7(b) for a comparison of the fractional anisotropy in D_{TI} and D_C for varying values of κ.

Eq. (21) is solved on a domain Ω describing a transverse slice of the CNS for an initially symmetric (circular) tumour:

$$c_0(x,y) = 0.1e^{-(x-x_0)^2}e^{-(y-y_0)^2},$$

where (x_0,y_0) defines its initial centre. We note that while the numerical simulations are performed on a rectangular grid we have imposed internal zero-flux boundaries to provide a (crude) description of a realistic brain geometry.

Fig. 7(c) plots the tumour evolution under varying values of κ: $\kappa = 0$ (i.e. the isotropic case), $\kappa = 5, 10$ and 20. In the isotropic case, tumour growth is uniform in all directions and only bounded by the finite extent of the simulated domain. Consistent with our analyses using synthetic datasets, for $\kappa > 0$ we observe
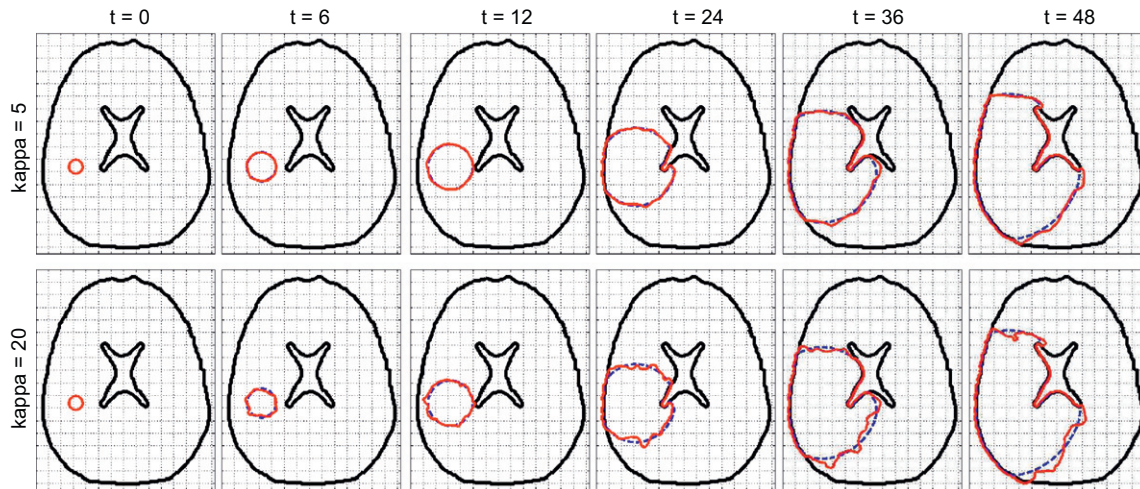
Fig. 8. Contour comparison showing impact of anisotropy on invasion. We compare anisotropic ($\kappa > 0$) simulations from Fig. 7 with the isotropic case ($\kappa = 0$) for (top row) $\kappa = 5$ and (bottom row) $\kappa = 20$. Contours mark the equal density lines for $c(x,y) = 0.001$ (i.e. 0.1% of the maximum density) for the isotropic (dashed blue line) and anisotropic (solid red line) simulations at the times (months) indicated above the top panel. Underlying grid lines mark 1 cm. Numerical details as for Fig. 7. (For interpretation of the references to color in this figure caption, the reader is referred to the web version of this article.)

anisotropic spread of the tumour, with increasingly nonuniform growth as κ is increased. In particular, we observe a much more variable spread in regions of higher anisotropy, such as the corpus callosum. The variation between the isotropic and anisotropic cases is revealed more clearly in Fig. 8 through comparing contours at distinct times.

6. Discussion

An accurate prediction of glioma extent and a confident suggestion for the treatment volume are of huge importance in their eradication, yet providing answers is greatly complicated by their phenotypic diversity and physical/chemical interactions with the surrounding environment. While a model that integrates all important factors presents a formidable mathematical and computational challenge, it is now possible to employ modelling to explore in depth the impact of specific interactions. In this paper we have focused on the role of the white matter fibre tracts on facilitating invasive spread. From previous research (Clatz et al., 2005; Bondiau et al., 2008; Konukoglu et al., 2010; Jbabdi et al., 2005; Cobzas et al., 2009; Mosayebi et al., 2011) we have identified a need for a model that translates measured DTI information into the inputs for a predictive and macroscopic model for tumour growth. Our modelling workflow is to parametrise the turning characteristics of an individual-level model according to standard anisotropy measurements (eigenvectors, fractional anisotropy) and employ scaling methods to derive the corresponding continuum model. We have demonstrated the utility of the approach through simulations on both artificial and genuine DTI datasets, echoing the findings of others by revealing how the environmental anisotropy inferred from DTI datasets can significantly impact on the invasive profile of the tumour.

Phenomenological reaction–diffusion based models, parametrised by clinical data, have proved highly accurate at predicting the form and rate glioma growth/invasion (for example, see the review of Harpold et al., 2007, and references therein). While the model here, derived from an explicit individual-level model, appears close in form to previously proposed anisotropic-diffusion based models (e.g. Clatz et al., 2005; Jbabdi et al., 2005; Cobzas et al., 2009; Mosayebi et al., 2011), we remark on some key distinctions. First, the framework here bridges local and global scales: we first proposed a mesoscopic scale model based on the individual-level migration response of a cell within some complex tissue architecture, and then employed scaling techniques to derive the corresponding macroscopic model for invasion of the tumour. Thus, the inputs for the macroscopic model parameters can be directly linked to explicit parameters, such as cell speeds and turning angle distributions. Second, the form of the macroscopic anisotropic-diffusion model is augmented by additional advective-type terms which can generate spatially varying cell density distributions as anisotropy in the environment varies. More generally, it is firmly established that the precise local (microscopic) rules imposed for how a cell chooses directions can have a huge bearing on the form of the macroscopic model (e.g. Othmer and Stevens, 1997). The current framework offers a pathway for deriving and comparing distinct forms of macroscopic models for glioma growth, according to distinct hypotheses for how a cell responds to the local information or structure of the environment.

The work here strips the fundamental equations down to their bare bones: we have aimed for the most transparent demonstration of the key ideas, rather than obscuring these details within a more sophisticated model. However, the framework is significantly more flexible and a number of important extensions can be considered in future iterations. For example, employing ideas from tractography may allow a connection from the DTI (and other imaging) datasets to an imposed tissue structure, with the cell movement directed according to features of this network (e.g. density and orientation of fibre tracts). Further, given the distortion to the CNS tissue network as the tumour expands, a time-evolving tissue architecture can also be imposed. Further areas for exploration include the switching of the behaviour of cells between a migratory/nonproliferative and stationary/proliferative, e.g. (Pham et al., 2012), the growing genetic instability of the tumour, or incorporating the impact of cell interactions/volume considerations on the movement dynamics of cells (Chauviere et al., 2007; Treloar et al., 2011).

The modelling framework itself is independent of the spatial dimension, however, we have generally concentrated on two dimensions for clarity. The numerical extension to three dimensions is algorithmically straightforward, however the additional numerical cost is high and the implementation of more efficient numerical algorithms would be advantageous for larger scale numerical studies. We briefly considered a trivial extension of the cell turning function for the three dimensional case, however closer scrutiny is demanded. In three dimensions, anisotropy of a diffusion tensor is represented by an ellipsoid, with its shape

determined by the lengths of its principal axes. Utilising only the eigenvector corresponding to the principal direction of anisotropy omits possibly crucial information on the projection into other directions. Solutions would be to consider the superposition of multiple von Mises–Fisher distributions, with their dominating directions aligned according to the three principal axes of the ellipsoid and weighted by their lengths, or more complicated distributions such as a Kent (1982) distribution.

Our principal aim at this stage has been to suggest a modelling framework which can subsequently be tailored and adapted as required. Consequently, the results presented should be taken to be illustrative of the methodology, rather than predictive. The next level of modelling, where more precise predictions are formulated, will necessarily demand a more robust and careful validation of the model through dedicated application and matching to clinical data.

Acknowledgements

Appendix A. Proofs

Case1: Peanut

Lemma 1. *Assume $\hat{q}$ is given by* (12). *Then the macroscopic diffusion tensor* (11) *is given by* (13).

Proof. To compute the macroscopic diffusion tensor $D_T(x)$, we use index notation and summation convention. We also omit space dependence for clarity.

$$D_C = \frac{s^2}{\mu} \int_{\mathbb{S}^{n-1}} \theta\theta^T \hat{q}(\theta)\, d\theta,$$

$$= \frac{ns^2}{\mu|\mathbb{S}^{n-1}|\operatorname{tr} D_{TI}} \int_{\mathbb{S}^{n-1}} \theta\theta^T \theta^T D_{TI}\theta\, d\theta.$$

Hence in coordinates we have

$$D_C^{kl} = \frac{ns^2}{\mu|\mathbb{S}^{n-1}|\operatorname{tr} D_{TI}} D_{TI,ij} \int_{\mathbb{S}^{n-1}} \theta^k \theta^l \theta^i \theta^j\, d\theta.$$

In an earlier paper (Hillen, 2005) an explicit general formula for arbitrary velocity moments has been calculated. From Lemma 2.2 in Hillen (2005) we have that

$$\int_{\mathbb{S}^{n-1}} \theta^k \theta^l \theta^i \theta^j\, d\theta = \frac{|\mathbb{S}^{n-1}|}{n(2+n)} (\delta^{kl}\delta^{ij} + \delta^{ki}\delta^{lj} + \delta^{kj}\delta^{il}).$$

Hence we find

$$D_C^{kl} = \frac{ns^2|\mathbb{S}^{n-1}|}{n(2+n)\mu|\mathbb{S}^{n-1}|\operatorname{tr} D_{TI}} D_{TI,ij}(\delta^{kl}\delta^{ij} + \delta^{ki}\delta^{lj} + \delta^{kj}\delta^{il}),$$

$$= \frac{s^2}{\mu(2+n)\operatorname{tr} D_{TI}} (\delta^{kl} \operatorname{tr} D_{TI} + D_{TI}^{kl} + D_{TI}^{lk}).$$

Since D_{TI} is symmetric, we obtain

$$D_C = \frac{s^2}{\mu(2+n)}\left(\mathbb{I} + \frac{2D_{TI}}{\operatorname{tr} D_{TI}}\right), \qquad (A.1)$$

where $\mathbb{I}$ denotes the identity matrix. □

Lemma 2. *Consider spatial dimensions $n=2$ and $n=3$. Assume D_{TI} is a given DTI measurement and D_C is given by* (13). *Then*

(a) $\operatorname{RA}(D_C) < 3$;

(b) $\operatorname{RA}(D_C) \le \operatorname{RA}(D_{TI})$ *and* $\operatorname{FA}(D_C) \le \operatorname{FA}(D_{TI})$. (A.2)

If a_l, a_p, a_s denote the linear, planar and spherical indices of D_{TI}, respectively, and $\tilde{a}_l, \tilde{a}_p, \tilde{a}_s$ are those of D_C, then

$$\tilde{a}_l = \tfrac{2}{3} a_l, \quad \tilde{a}_p = \tfrac{2}{3} a_p, \quad \tilde{a}_s = 1 + \tfrac{2}{3}a_s.$$

Hence the resulting ellipsoid is less anisotropic and more spherical shaped.

Proof. We prove the above statements for spatial dimension $n=3$; the results for $n=2$ are very similar. Let $\lambda_1 \ge \lambda_2 \ge \lambda_3$ denote the eigenvalues of D_{TI} and we abbreviate $\operatorname{tr} := \lambda_1 + \lambda_2 + \lambda_3$ with $\operatorname{tr} > 0$. Then the eigenvalues of D_C are given by

$$\tilde{\lambda}_j = \frac{s^2}{\mu(2+n)}\left(1 + \frac{2\lambda_j}{\operatorname{tr}}\right), \quad j = 1,2,3.$$

To prove statement (a) we write for $j \neq 1$

$$\frac{\tilde{\lambda}_1}{\tilde{\lambda}_j} = \frac{1 + \dfrac{2\lambda_1}{\operatorname{tr}}}{1 + \dfrac{2\lambda_j}{\operatorname{tr}}} = \frac{\operatorname{tr} + 2\operatorname{tr} - 2\sum_{i=2}^{n}\lambda_i}{\operatorname{tr} + 2\lambda_j},$$

$$= 3\frac{\operatorname{tr}}{\operatorname{tr} + 2\lambda_j} - 2\frac{\sum_{i=2}^{n}\lambda_i}{\operatorname{tr} + 2\lambda_j},$$

$$< 3,$$

if all $\lambda_j > 0$. The anisotropy can only equal 3, if $\lambda_j = 0$ for all $j > 1$. To show the first statement of (b), we reformulate the above formula slightly:

$$\frac{\tilde{\lambda}_1}{\tilde{\lambda}_j} = \frac{\operatorname{tr}/\lambda_j + 2\lambda_1/\lambda_j}{\operatorname{tr}/\lambda_j + 2},$$

which is less than λ_1/λ_j for $\lambda_1 > \lambda_j$. For the second formula of item (b), we compute the fractional anisotropy of D_C as

$$\operatorname{FA}(D_C) = \frac{\sqrt{(\lambda_1 - \lambda_2)^2 + (\lambda_1 - \lambda_3)^2 + (\lambda_2 - \lambda_3)^2}}{\sqrt{2[(\operatorname{tr}/2 + \lambda_1)^2 + (\operatorname{tr}/2 + \lambda_2)^2 + (\operatorname{tr}/2 + \lambda_3)^2]}} < \operatorname{FA}(D_{TI}).$$

To compute the shape indices $\tilde{a}_l, \tilde{a}_p, \tilde{a}_s$, we need the trace of D_C:

$$\tilde{\operatorname{tr}} := \frac{3s^2}{\mu(n+2)}.$$

Then the above formulae follow directly from the definition of the indices:

$$\tilde{a}_l = \frac{\tilde{\lambda}_1 - \tilde{\lambda}_2}{\tilde{\operatorname{tr}}}, \quad \tilde{a}_p = \frac{2(\tilde{\lambda}_2 - \tilde{\lambda}_3)}{\tilde{\operatorname{tr}}}, \quad \tilde{a}_s = \frac{3\tilde{\lambda}_3}{\tilde{\operatorname{tr}}}. \qquad □$$

Case2: Bimodal von Mises distribution

Lemma 3. *Assume D_{TI} denotes a measured water diffusion tensor in two dimensions and D_C is defined by* (18). *Let λ_1, λ_2 denote the eigenvalues of D_{TI} and $\tilde{\lambda}_1, \tilde{\lambda}_2$ those of D_C. Then*

(A) $\tilde{\lambda}_1 = \dfrac{s^2}{2\mu}\left(1 + (1-\delta)\dfrac{I_2(k)}{I_0(k)}\right),$

  $\tilde{\lambda}_2 = \dfrac{s^2}{2\mu}\left(1 - (1-\delta)\dfrac{I_2(k)}{I_0(k)}\right),$

(B) $\operatorname{RA}(D_C) = \dfrac{1 + (1-\delta)\dfrac{I_2(k)}{I_0(k)}}{1 - (1-\delta)\dfrac{I_2(k)}{I_0(k)}},$

(C) $FA(D_C) = \dfrac{2(1-\delta)\dfrac{I_2(k)}{I_0(k)}}{\sqrt{2+2(1-\delta)^2\left(\dfrac{I_2(k)}{I_0(k)}\right)^2}}.$

(D) $\tilde{a}_l = (1-\delta)\dfrac{I_2(k)}{I_0(k)}, \quad \tilde{a}_p = 1-\tilde{a}_l.$

Proof. It should be noted that eigenvectors φ_1, φ_2 of D_{TI} are also eigenvectors of D_C. Since they are orthogonal the above formulae follow through straightforward computations from (18).   □

Remarks.

1. The ratio of modified Bessel functions $I_2(k)/I_0(k)$ is a monotonically increasing function with $I_2(0)/I_0(0) = 0$ and $\lim_{k\to\infty} I_2(k)/I_0(k) = 1$.
2. The anisotropy of D_C depends on the choices of δ and k and in the limit of $\delta \to 0$ and $k \to \infty$ we obtain

$$\tilde{\lambda}_1 \to s^2/\mu, \quad \tilde{\lambda}_2 \to 0,$$

and

$$RA(D_C) \to +\infty, \quad FA(D_C) \to 1.$$

Hence there is no limit in the anisotropy of D_C.

Appendix B. Numerical method

Simulations have been performed for 2D domains, however, the scheme trivially extends to 3D (albeit at increased computational expense). To solve Eq. (21) we employ a Method of Lines approach, discretising in space with a suitable finite-difference approximation (below) to obtain a system of time-dependent ODEs. We consider the 2D regular domain $(x,y) \in \Omega = [0,L_x] \times [0,L_y]$ and discretise it into a regular lattice with grid coordinates at $x_1 = \Delta_x/2,\ x_2 = 3\Delta_x/2 \ldots x_M = L_x - \Delta_x/2,\ y_1 = \Delta_y/2,\ y_2 = 3\Delta_y/2 \ldots y_N = L_y - \Delta_y/2$ for $\Delta_x = L_x/M,\ \Delta_y = L_y/N$. In 2D, assuming the (positive definite and symmetric) tensor matrix takes the form:

$$D_C(x,y) = \begin{pmatrix} \alpha(x,y) & \beta(x,y) \\ \beta(x,y) & \gamma(x,y) \end{pmatrix},$$

we observe that spatial terms on the right-hand side of (21) can be expanded as follows:

$$\nabla\nabla(D_C c(x,y)) = (\alpha(x,y)c_x)_x + (\beta(x,y)c_x)_y + (\beta(x,y)c_y)_x + (\gamma(x,y)c_y)_y$$
$$+ (\alpha(x,y)_x c)_x + (\beta(x,y)_y c)_x + (\beta(x,y)_x c)_y + (\gamma(x,y)_y c)_y.$$

This reveals a combination of diffusive (first line) and advective (second line) type-terms, with the diffusive terms in the first line identical to those generated for standard anisotropic diffusion (2).

It is important to note that the choice for the finite-difference discretisation of the diffusive terms is crucial: naive discretisations can potentially generate numerical instability through negative β, see Mosayebi et al. (2010). To account for this, we employ the finite discretisation method of Weickert (1998), where approximations of the derivatives are calculated not only in the "standard" directions, but combined with those calculated in an appropriately chosen new direction. For the advective terms we discretise in conservative form, employing a first-order upwinding scheme.

We implement zero-flux boundary conditions: for the simulations using genuine DTI data, these are imposed on the internal boundaries that approximate the brain geometry. All numerical simulations presented employ a simple forward Euler method for the time discretisation of the ODE system with a suitably small

time-step Δt, although more sophisticated algorithms (e.g. implicit, variable time-stepping) have also been employed with equivalent behaviour observed. To verify the numerical method, simulations have been performed for varying time-step and mesh-discretisations.

References

Basser, P.J., 2008. Diffusion and diffusion tensor MR imaging: fundamentals. In: Atlas, S.W. (Ed.), Magnetic Resonance Imaging of the Brain and Spine. Lippincott Williams, Philadelphia, pp. 1752–1767 (Chapter 31).

Bondiau, P.Y., Clatz, O., Sermesant, M., Marcy, P.Y., Delingette, H., Frenay, M., Ayache, N., 2008. Biocomputing: numerical simulation of glioblastoma growth using diffusion tensor imaging. Phys. Med. Biol. 53, 879–893.

Chauviere, A., Hillen, T., Preziosi, L., 2007. Modeling cell movement in anisotropic and heterogeneous network tissues. Networks Hetero. Media 2, 333.

Clatz, O., Sermesant, M., Bondiau, P.Y., Delignette, H., Warfield, S.K., Malandain, G., Ayache, N., 2005. Realistic simulation of the 3D growth of brain tumors in MRI images coupling diffusion with biomechanical deformation. IEEE Trans. Med. Imaging 24, 1334–1346.

Cobzas, D., Mosayebi, P., Murtha, A., Jagersand, M., 2009. Tumour invasion margin on the Riemannian space of brain fibers. In: International Conference on Medical Image Computing and Computer Assisted Intervention (MICCAI).

Dunn, G.A., Heath, J.P., 1976. A new hypothesis of contact guidance in tissue cells. Exp. Cell Res. 101, 1–14.

Evans, L.C., 1998. Partial Differential Equations. American Mathematical Society, Providence, RI.

Giese, A., Bjerkvig, R., Berens, M.E., Westphal, M., 2003. Cost of migration: invasion of malignant gliomas and implications for treatment. J. Clin. Oncol. 21, 1624–1636.

Giese, A., Kluwe, L., Laube, B., Meissner, H., Berens, M.E., Westphal, M., 1996. Migration of human glioma cells on myelin. Neurosurgery 38, 755–764.

Guido, S., Tranquillo, R.T., 1993. A methodology for the systematic and quantitative study of cell contact guidance in oriented collagen gels. Correlation of fibroblast orientation and gel birefringence. J. Cell Sci. 105, 317–331.

Harpold, H.L.P., Alvord Jr., E.C., Swanson, K.R., 2007. The evolution of mathematical modeling of glioma proliferation and invasion. J. Neuropathol. Exp. Neurol. 66, 1–9.

Haston, W.S., Shields, J.M., Wilkinson, P.C., 1983. The orientation of fibroblasts and neutrophils on elastic substrata. Exp. Cell Res. 146 (1), 117–126.

Hatzikirou, H., Deutsch, A., Schaller, C., Simaon, M., Swanson, K., 2005. Mathematical modelling of glioblastoma tumour development: a review. Math. Models Methods Appl. Sci. 15, 1779–1794.

Hillen, T., 2005. On the L^2-closure of transport equations: the general case. Disc. Contin. Dyn. Syst. B 5, 299–318.

Hillen, T., 2006. M^5: mesoscopic and macroscopic models for mesenchymal motion. J. Math. Biol. 53, 585–616.

Hillen, T., Hinow, P., Wang, Z.A., 2010. Mathematical analysis of a kinetic model for cell movement in network tissues. Disc. Contin. Dyn. Syst. B 14, 1055–1080.

Hillen, T., Painter, K.J., 2013. Transport and anisotropic diffusion models for movement in oriented habitats. In: Lewis, M., Maini, P., Petrovskii, S. (Eds.), Dispersal, Individual Movement and Spatial Ecology: A Mathematical Perspective. Springer, Heidelberg.

Hillen, T., Painter, K.J., 2013. Moments of von Mises–Fisher distributions. In preparation.

Hillen, T., Painter, K.J., Winkler, M., 2013. Anisotropic diffusion in oriented environments can lead to singularity formation. Eur. J. Appl. Math., http://dx.doi.org/10.1017/S0956792512000447.

Jbabdi, A., Mandonnet, E., Duffau, H., Capelle, L., Swanson, K.R., Pelegrini-Issac, M., Guillevin, R., Benali, H., 2005. Simulation of anisotropic growth of low-grade gliomas using diffusion tensor imaging. Magn. Reson. Med. 54, 616–624.

Jiang, H., van-Zijl, P.C., Kim, J., Pearlson, G.D., Mori, S., 2006. DtiStudio: resource program for diffusion tensor computation and fiber bundle tracking. Comput. Methods Programs Biomed. 81, 106–116.

Kent, J.T., 1982. The Fisher-Bingham distribution on the sphere. J. R. Stat. Soc. 44, 71–80.

Kettemann, A., 2010. Mathematical Modelling and Numerical Simulation of Chemosensitive Cell Dynamics in Multidimensional Tissue Networks. Ph.D. Thesis. Shaker Verlag, Univ Stuttgart.

Konukoglu, E., Clatz, O., Bondiau, P.Y., Delignette, H., Ayache, N., 2010. Extrapolation glioma invasion margin in brain magnetic resonance images: suggesting new irradiation margins. Med. Image Anal. 14, 111–125.

Lenglet, C., Deriche, R., Faugeras, O., 2004. Inferring white matter geometry from diffusion tensor MRI: application to connectivity mapping. Lecture Notes in Computer Science 3024, 127–140.

Mandonnet, E., Pallud, J., Clatz, O., Taillandier, L., Konukoglu, E., Duffau, H., Capelle, L., 2008. Computational modeling of the who grade ii glioma dynamics: principles and applications to management paradigm. Neurosurg. Rev. 31, 263–269.

Mardia, K.V., Jupp, P.E., 2000. Directional Statistics. Wiley and Sons.

Mosayebi, P., Cobzas, D., Jagersand, M., Murtha, A., 2010. Stability effects of finite difference methods on a mathematical tumor growth model. In: Computer

Vision and Pattern Recognition Workshops (CVPRW), 2010 IEEE Computer Society Conference. IEEE Conference Proceedings, pp. 125–132.

Mosayebi, P., Cobzas, D., Murtha, A., Jagersand, M., 2011. Tumor invasion margin on the Riemannian space of brain fibers. Med. Image Anal. 16, 361–373.

O'Dennell, L., Haker, S., Westin, C.F., 2002. New approaches to estimation of white matter connectivity in diffusion tensor MRI: elliptic PDEs and geodesics in a tensor-warped space. Lecture Notes in Computer Science 2488, 459–466.

Othmer, H.G., Stevens, A., 1997. Aggregation, blowup and collapse: the ABC's of taxis in reinforced random walks. SIAM J. Appl. Math. 57, 1044–1081.

Painter, K.J., 2009. Modelling migration strategies in the extracellular matrix. J. Math. Biol. 58, 511–543.

Pham, K., Chauviere, A., Hatzikirou, H., Li, X., Byrne, H.M., Cristini, V., Lowengrub, J., 2012. Density-dependent quiescence in glioma invasion: instability in a simple reaction–diffusion model for the migration/proliferation dichotomy. J. Biol. Dyn. 6, 54–71.

Rohmer, D., Gullberg, G.T., 2006. A Bloch-Torrey Equation for Diffusion in Deforming Media. Technical Report, Lawrence Berkeley National Lab, pp. 1–19.

Swanson, K.R., Bridge, C., Murray, J.D., Alvord Jr., E.C., 2003. Virtual and real brain tumors: using mathematical modeling to quantify glioma growth and invasion. J. Neurol. Sci. 216, 1–10.

Swanson, K.R., Alvord Jr., E.C., Murray, J.D., 2000. A quantitative model for differential motility of gliomas in grey and white matter. Cell Prolif. 33, 317–329.

Treloar, K.K., Simpson, M.J., McCue, S.W., 2011. Velocity-jump models with crowding effects. Phys. Rev. E 84, 061920.

Weickert, J., 1998. Anisotropic Diffusion in Image Processing. Teubner, Stuttgart.

Wolf, K., Muller, R., Borgmann, S., Brocker, E.B., Friedl, P., 2003. Amoeboid shape change and contact guidance: T-lymphocyte crawling through fibrillar collagen is independent of matrix remodeling by MMPs and other proteases. Blood 102, 3262–3269.

Wood, A., Thorogood, P., 1984. An analysis of in vivo cell migration during teleost fin morphogenesis. J. Cell. Sci. 66, 205–222.